



HAL
open science

Satellite data-based 3D simulation of Kelvin-Helmholtz instability and induced magnetic reconnection at the Earth's magnetopause

M Sisti, Matteo Faganello, F. Califano, B. Lavraud

► **To cite this version:**

M Sisti, Matteo Faganello, F. Califano, B. Lavraud. Satellite data-based 3D simulation of Kelvin-Helmholtz instability and induced magnetic reconnection at the Earth's magnetopause. *Geophysical Research Letters*, In press. hal-02315872

HAL Id: hal-02315872

<https://hal.science/hal-02315872>

Submitted on 14 Oct 2019

HAL is a multi-disciplinary open access archive for the deposit and dissemination of scientific research documents, whether they are published or not. The documents may come from teaching and research institutions in France or abroad, or from public or private research centers.

L'archive ouverte pluridisciplinaire **HAL**, est destinée au dépôt et à la diffusion de documents scientifiques de niveau recherche, publiés ou non, émanant des établissements d'enseignement et de recherche français ou étrangers, des laboratoires publics ou privés.

1 **Satellite data-based 3D simulation of Kelvin-Helmholtz**
2 **instability and induced magnetic reconnection at the**
3 **Earth's magnetopause**

4 **M. Sisti^{1,2}, M. Faganello¹, F. Califano², and B. Lavraud³**

5 ¹Aix-Marseille University, CNRS, PIIM UMR 7345 - Marseille, France

6 ²Physics Department, University of Pisa - Pisa, Italy

7 ³IRAP, University of Toulouse, CNRS, CNES, UPS - Toulouse, France

8 **Key Points:**

- 9 • We present a 3D two-fluid simulation using plasma parameters as measured by
10 MMS on September 8th 2015
- 11 • We observe that vortex induced and mid-latitude magnetic reconnection coexist
- 12 • We estimate the effective diffusion coefficient associated with reconnection, ob-
13 taining $D_{eff} \simeq 10^{10} \text{ m}^2/\text{s}$, large enough to explain the observed mixing

Abstract

We present a 3D two-fluid simulation using plasma parameters as measured by MMS on September 8th 2015 concerning the nonlinear development of the Kelvin-Helmholtz instability at the Earth's magnetopause. We observe an extremely rich nonlinear dynamics including the development of a complex magnetic topology, vortex merging and secondary KH instability driven by large-scale vortices distributed asymmetrically in latitude. Vortex induced and mid-latitude magnetic reconnection coexist and produce an asymmetric distribution of magnetic reconnection events. These results are in good agreement with MMS observations on the same day, in particular for the presence of both equatorial and off-equator reconnection. Regarding the latter only we note a predominance of reconnection in the southern hemisphere during the early nonlinear phase. The estimated effective diffusion coefficient associated with the dynamics is found to be large enough to account for the observed mass transport at the Earth's magnetospheric flanks.

1 Introduction

Several decades of studies definitely proved the key role played by the Kelvin-Helmholtz instability (KHI) in regulating plasma transport from the solar wind (SW) into planetary magnetospheres. In particular, satellite data collected around the Earth's magnetopause revealed the presence of rolled-up KH vortices (Hasegawa et al., 2004) under a variety of SW magnetic field orientations (Hasegawa et al., 2006; Hwang et al., 2011; Farrugia et al., 2014; Kavosi & Raeder, 2015) and the direct proof of magnetic reconnection events forced by the vortices themselves (Hasegawa et al., 2009; Eriksson et al., 2016). This proof is of paramount importance since KH vortices alone cannot explain the observed transport. Vortices develop as large-scale, nearly magnetohydrodynamic (MHD) structures that strongly perturb and fold the magnetopause but preserve the magnetic topology. Thus, they cannot induce an effective transport (Foullon et al., 2008; Nykyri & Otto, 2001). In contrast, new open field lines emerging from reconnection events allow particles to stream from the SW into the magnetosphere leading to direct plasma entry (Nakamura & Daughton, 2014; Daughton et al., 2014). This kind of dynamics is of great interest also for planetary magnetospheres (Johnson et al., 2014) and magnetized astrophysical objects characterized by the presence of strong velocity gradients (Lovelace et al., 2010; Li & Narayan, 2004).

45 Here we focus our analysis on northward Interplanetary Magnetic Field (IMF) pe-
46 riods at Earth when the magnetic field advected by the SW is mainly parallel to the mag-
47 netospheric one at low-latitude, but including a rotation in the transition from the SW
48 to the magnetosphere. In this region KH vortices can effectively grow with wavevectors
49 nearly perpendicular to the average magnetic field minimizing the effect of magnetic ten-
50 sion, but still fairly aligned with the flowing SW maximizing the velocity shear driver
51 (Faganello & Califano, 2017; Southwood, 1968; Walker, 1981; Miura & Pritchett, 1982).
52 If an initial magnetic rotation is taken into consideration, the associated current sheet
53 is pinched in between vortices and Type I Vortex Induced Reconnection (VIR) is forced
54 on the ideal KH time-scale, faster than the usual reconnection one (Chen & Morrison,
55 1990; Knoll & Chacón, 2002). VIR creates “open” field lines crossing the magnetopause
56 eventually producing the development of a mixing layer (Nakamura et al., 2013). At mag-
57 netopause flanks, the KHI is gradually stabilized at higher latitudes (Farrugia et al., 1998;
58 Gratton et al., 2003; Contin, 2003). As a result magnetic field lines are advected differ-
59 ently at low latitude, once engulfed in vortices, and at high latitudes where the flow is
60 more and more unperturbed. In such a way, even if IMF and magnetospheric field lines
61 are aligned, so that no magnetic rotation is present, mid-latitude current sheets are cre-
62 ated where reconnection finally occurs (Faganello, Califano, Pegoraro, & Andreussi, 2012;
63 Borgogno et al., 2015). Proceeding at the same time in both hemispheres, mid-latitude
64 reconnection (MLR) is able to create twice-reconnected, “newly closed” field lines con-
65 nected to the Earth at both poles while embedded within SW plasma at low-latitude.
66 Twice-reconnected field lines allow for a direct and effective injection of SW plasma into
67 the magnetosphere (Faganello, Califano, Pegoraro, & Andreussi, 2012; Johnson & Wing,
68 2009). Measurements of *remote* reconnection signatures using electron particle fluxes have
69 been reported by Cluster (Bavassano Cattaneo et al., 2010), Themis (Faganello et al.,
70 2014) and MMS (Vernisse et al., 2016). In these works the location of reconnection sites
71 is inferred by looking at the angle of detected suprathermal particles with respect to lo-
72 cal magnetic field: parallel particle fluxes are related to events occurring in the south-
73 ern hemisphere, while antiparallel fluxes come from events in the northern one. Inter-
74 estingly, MMS observations on September 8th 2015 indicate that VIR proceeding at equa-
75 torial latitude and MLR coexist (Eriksson et al., 2016; Vernisse et al., 2016). MMS was
76 located close to the GSE equatorial plane where vortices and *in-situ* VIR outflows were
77 detected. At the same time satellites observed parallel and antiparallel particle fluxes

78 as signatures of *remote* reconnection, with more events with parallel fluxes. This fact sug-
79 gests that the latitudinal distribution of *remote* reconnection events was asymmetric, with
80 more events located in the southern hemisphere rather than in the northern one. This
81 dynamics have been confirmed by numerical simulations taking into account high-latitude
82 stabilization as well as the initial magnetic rotation (Fadanelli et al., 2018), but not the
83 actual magnetic/plasma parameters of the observed MMS event. The magnetic rotation
84 breaks the reflection symmetry with respect to the equatorial plane so that the system
85 evolves differently in the two hemispheres. As a consequence, MLR and the production
86 of twice-reconnected lines could be affected (Fadanelli et al., 2018; Ma et al., 2017). At
87 the same time local kinetic simulations of this MMS event have been performed focus-
88 ing on VIR only (Nakamura, Hasegawa, et al., 2017; Nakamura, Eriksson, et al., 2017),
89 showing that VIR can become turbulent producing a layer where different particle pop-
90 ulations are effectively mixed-up, with a local entry rate comparable with that required
91 for the observed mass transfer during northward IMF periods (Sonnerup, 1980). How-
92 ever, for such simulations, the numerical box has a limited size in latitude, thus they can-
93 not reproduce the *remote* dynamics of MLR.

94 Here we analyze a 3D two-fluid simulation using the parameters measured during
95 the MMS event of September 8th 2015 and a large enough numerical box in order to in-
96 clude high-latitude stabilization. We show, in agreement with MMS observations, that
97 VIR and MLR coexist and determine the complex magnetic field topology. To summa-
98 rize: i) even if the symmetry of mid-latitude reconnection is broken by the presence of
99 the large scale magnetic field rotation, the production of twice-reconnected field lines is
100 still efficient, ii) the effective diffusion coefficient associated with such a complex topol-
101 ogy can explain the observed transport in a wide latitude range, iii) the asymmetry of
102 reconnection events reproduces that observed during the MMS event on which the sim-
103 ulation parameters are set, iv) the late nonlinear phase is extremely rich with vortex merg-
104 ing and the development of secondary KH instability that boost the production of re-
105 connected lines and the effective diffusivity. Our simulation is able to account for the main
106 features characterizing the dynamics as inferred from MMS data on September 8th 2015
107 (Eriksson et al., 2016; Vernisse et al., 2016) and predicts an even more complex evolu-
108 tion of the magnetic topology when moving tailward as compared to the satellite posi-
109 tion.

2 Plasma model and simulation setup

We consider a slab geometry with the x -axis perpendicular to the magnetopause, z as the latitude and the y -axis along the SW flow. The plasma evolution is described by a two-fluid set of equations:

$$\partial_t n + \nabla \cdot (n\mathbf{U}) = 0 \quad ; \quad n = n_i \simeq n_e \quad (1)$$

$$\partial_t(n\mathbf{U}) + \nabla \cdot \left[n\mathbf{U}\mathbf{U} + (P_i + P_e + B^2/2)\bar{\mathbf{I}} - \mathbf{B}\mathbf{B} \right] = 0 \quad (2)$$

$$\partial_t(nS_j) + \nabla \cdot (nS_j\mathbf{u}_j) = 0 \quad ; \quad S_j = P_j n^{-5/3} \quad ; \quad j = i, e \quad (3)$$

where n is the plasma density, $\mathbf{u}_i \simeq \mathbf{U}$ the ion fluid velocity, $\mathbf{u}_e = \mathbf{U} - \mathbf{J}/n$ the electron fluid velocity, $\mathbf{J} = \nabla \times \mathbf{B}$ the current density and P_j , $j = i, e$, the pressures. All quantities are normalized using the ion mass and charge, the ion skin depth d_i and the z -component of the Alfvén velocity at the center of the simulation domain. The Faraday equation and a generalized Ohm’s law,

$$\mathbf{E} = -\mathbf{u}_e \times \mathbf{B} - \frac{1}{n} \nabla P_e + \eta \mathbf{J}, \quad (4)$$

complete the set. We use a small but finite resistivity $\eta = 10^{-3}$, corresponding to a resistive diffusion time scale $\tau_R \simeq \eta^{-1} a^2 \simeq 10^4$, associated with the equilibrium scale length a , which is far bigger than the simulation time. As a consequence the magnetic field is frozen-in to the large-scale KH motion and we don’t observe any appreciable magnetic diffusion until reconnection starts in d_i -scale current sheets. Here reconnection is expected to develop on a time scale nearly independent of the η value as for Hall-dominated reconnection (Birn et al., 2001). Even if a kinetic model would better reproduce the finer structures of magnetic reconnection, our description is nevertheless able to capture the correct reconnection time-scale in the complex 3D evolution of KHI and to describe the evolution of the global magnetic topology (Faganello, Califano, Pegoraro, & Andreussi, 2012). We model the initial large-scale configuration by using a 2D Grad-Shafranov equilibrium that includes the strong gradients across the magnetopause and reproduces the high-latitude stabilization along z (Faganello, Califano, Pegoraro, Andreussi, & Benkadda, 2012). All equilibrium quantities are obtained by a flux function

$$\psi(x, z, t = 0) = \frac{2}{3}x + \frac{1}{3} \frac{L_z}{2\pi} \sinh \frac{2\pi x}{L_z} \cos \frac{2\pi z}{L_z} \quad (5)$$

133 giving $\mathbf{B}_{eq} = \nabla\psi \times \hat{\mathbf{y}} + (B_{flow}/2) [1 + \tanh(\psi/a)]\hat{\mathbf{y}}$, $n_{eq} = 1 + (\Delta n/2) \tanh(\psi/a)$,
 134 $\mathbf{U}_{eq} = (\Delta U/2) \tanh(\psi/a)\hat{\mathbf{y}}$, $P_{i,eq} + P_{e,eq} + B_{eq,y}^2/2 = (P_{i,eq} + P_{e,eq} + B_{eq,y}^2/2)|_{\psi=0}$ with
 135 $P_{i,eq} = 4 P_{e,eq}$. Here B_{flow} is the flow-aligned component of the IMF that, adding to
 136 the northward component of the magnetic field, reproduces its rotation. We take equi-
 137 librium quantities compatible with the MMS event, as given by the values reported in
 138 the outer magnetosphere and in the adjacent magnetosheath in the auxiliary material
 139 of Eriksson et al. (2016). In particular n varies from $5.7cm^{-3}$ to $20.1cm^{-3}$, with an av-
 140 eraged value of $\sim 13cm^{-3}$. Using this value when normalizing, we have $n = 1$ at the
 141 magnetopause and $\Delta n = 1$. The GSE z -component of the magnetic field is nearly con-
 142 stant at $\sim 67nT$ while the flow aligned component in the sheath is $\sim -24nT$. The ve-
 143 locity jump is $\sim 350km/s$. As a consequence normalized quantities read $B_{z,eq}|_{\psi=0} =$
 144 1 , $B_{flow} = -0.3$ and $\Delta U = 0.9$. The thermal temperature varies from $T_{th} = T_i +$
 145 $T_e = 2638eV + 124eV \sim 2800eV$ to $T_{th} = T_i + T_e = 189eV + 36eV \sim 200eV$; thus the
 146 averaged thermal temperature is $\sim 1500eV$ and $(P_{i,eq} + P_{e,eq})|_{\psi=0} = 0.9$. The pres-
 147 sure equilibrium condition given above reproduces a temperature jump across the mag-
 148 netopause of $\sim 2080eV$, slightly less but consistent with the MMS data. We set $a =$
 149 3 so that the fastest growing mode (FGM) wavelength $\lambda_{FGM} \simeq 4\pi a$ is big as compared
 150 to d_i and KH vortices develop at MHD scales. The box size is given by $L_x = 90 \simeq 2.4\lambda_{FGM}$,
 151 $L_y = 24\pi = 2\lambda_{FGM}$, $L_z = 96\pi = 8\lambda_{FGM}$. The number of grid points is $n_x = 600$,
 152 $n_y = n_z = 512$. All details on the numerical code, including transparent boundary
 153 conditions, can be found in Fadanelli et al. (2018) and references therein.

154 3 Data analysis

155 In Fig.1, panel *a*, we show a 3D rendering of the KH vortices at $t = 525$. Vortices
 156 develop around the equator while high-latitude regions are stable. The vortex axis, as
 157 shown by the folded shaded surface of the magnetopause, is tilted with respect to $\hat{\mathbf{z}}$ since
 158 the FGM wavevector is nearly perpendicular to the average \mathbf{B}_{eq} in the central region.
 159 This tilting is also underlined by the three central planes drawn perpendicularly to the
 160 vortex axis. As expected for $B_{flow} < 0$ (Fadanelli et al., 2018), vortices are more in-
 161 tense above the equatorial plane since the differential advection of field lines enhances
 162 the magnetic rotation in the southern hemisphere and lower it in the northern one. In-

163 deed, as shown in panel *b*, $\max_{(x,y)}(|J_{\parallel}|)$ (the maximum is searched in the entire xy -plane)
 164 as a function of z becomes larger and larger in the southern hemisphere (here $J_{\parallel} = \mathbf{J} \cdot$
 165 $\mathbf{B}/|\mathbf{B}|$). Since the presence of a magnetic rotation tends to stabilize the KHI (see panel
 166 *b*), the vortices are favoured above $z = 0$ (panel *c*) where $\max_{(x,y)}(u_{ix})$ is larger in the
 167 northern hemisphere. Panels *d*, *e*, *f* show density isocountours at different stages of the
 168 vortex evolution above the equator (at $z = 68$, close to the latitude where the vortices
 169 are more intense): at $t = 500$ when vortices are fully rolled-up, at $t = 600$ when they
 170 start to merge (Miura, 1997), at $t = 725$ when a single large-scale vortex has formed
 171 while small-scale secondary KHI (Matsumoto & Hoshino, 2004; Smyth, 2003) develops
 172 at the low-density boundary of the vortex where strong velocity gradients exists. At $z =$
 173 -30 (where the current peaks) KH nonlinear evolution proceeds in similar way (slightly
 174 less intense rolled-up vortices that finally merge), but no sign of secondary KHI appears,
 175 probably due to the enhanced magnetic shear. The evolution of $|J_{\parallel}|$ suggests that VIR
 176 should occur close to the equatorial plane at $t \sim 500$ where a single broad current peak
 177 is generated by the vortex pinching of the initial current sheet, see panel *b*, continuous
 178 line. Later on, at $t = 600$ a secondary current peak is visible at $z \sim 100$ so that MLR
 179 is expected to occur in the northern hemisphere (dashed line), while the main broad peak,
 180 although shifted southward by differential advection, would remain linked to VIR. Since
 181 reconnection in a 3D geometry is not trivial to be identified, we follow the ideal MHD
 182 evolution of the initial magnetic surfaces by integrating in time $\partial_t \psi + \mathbf{U} \cdot \nabla \psi = 0$. At
 183 $t = 0$ $|\psi|$ measures the distance from the (perturbed) magnetopause, with $\psi \simeq x$ around
 184 $z = 0$.

185 To look at reconnected field lines, we trace at given times a set of 22500 magnetic
 186 field lines whose feet are uniformly distributed in the (x, y) region $[-15, 15] \times [0, L_y]$ at
 187 $z = -L_z/2$. We define a line as “reconnected” when ψ has a jump along the line of at
 188 least $\pm a/2$ across the magnetopause. “Once-reconnected” lines have only one jump, “twice-
 189 reconnected” lines have two jumps, and we call “2⁺-reconnected” lines with three or more
 190 jumps. In order to provide a visual representation of the previous definitions, in Fig.2,
 191 panel *a*, we plot the value of ψ along two chosen magnetic field lines. One is once-reconnected
 192 and has a single ψ -jump around $z \lesssim 0$, while the other is twice-reconnected having a
 193 second jump around $z \sim 100$. Note that around both latitudes, where the connection
 194 changes occur, we observe clear ion and electron outflows pointing away from the site
 195 where the parallel current is maximal and where reconnection is proceeding (see Fig. S1

196 and S2 of Supporting Information). Signatures of the Hall quadrupole are visible below
 197 $z = 0$, even if quite distorted because of the “guide field” effect (Eastwood et al., 2010)
 198 and of the density asymmetry across the current sheet (Pritchett, 2008). A kinetic de-
 199 scription would probably reduce the distortion associated with the density asymmetry
 200 since particles streaming along reconnected field lines would rapidly smooth out density
 201 variations (Sturmer et al., 2018). At $z \sim 100$ the magnetic fluctuations due to the KH
 202 vortex strengthen, suppressing possible quadrupolar signatures (see Fig. S3 and S4 of
 203 Supporting Information).

204 For all field lines having a jump in ψ we record the latitude at which they cross the
 205 magnetopause in order to obtain a latitudinal distribution of sites of connection changes
 206 (Fig.2, panel *b*). At $t = 525$ this distribution is peaked just below $z = 0$ where VIR
 207 has created once-reconnected field lines. At $t = 600$ a second bump around $z \sim 100$
 208 is present corresponding to lines having reconnected a second time in the northern cur-
 209 rent peak due to MLR. The main peak associated with VIR has moved southward, as
 210 the main current peak did. These dynamics are confirmed by the temporal evolution of
 211 the number of once- or twice-reconnected lines, see Fig.2, panel *c*. At the beginning only
 212 once-reconnected lines are present and their number increases in time. After a while they
 213 reconnect a second time at mid latitude (in correspondence of the northern current peak,
 214 not shown) and the number of twice-reconnected lines increases too. The ratio between
 215 once- and twice-reconnected lines slowly increases in time (panel *d*) until $t \sim 675$ sug-
 216 gesting that the dynamics favour an efficient conversion from once- to twice-reconnected
 217 lines. After $t \sim 675$ this ratio reaches a plateau corresponding to nearly 60% of twice-
 218 reconnected lines. Even if not all once-reconnected lines reconnect a second time, the num-
 219 ber of lines doing this is far from being negligible. The production rate of twice-reconnected
 220 line is smaller by a factor of three than in the case without an initial magnetic rotation
 221 (Borgogno et al., 2015) but is of the same order of magnitude. The number of 2^+ -reconnected
 222 lines stays negligible.

223 Reconnection leads to the development of a mixing layer across the magnetopause
 224 where field lines have different topologies, from the original one, to “open” connection
 225 and “newly closed” ones. Because the mixing between the different populations is dom-
 226 inated by parallel streaming along reconnected lines (Daughton et al., 2014; Nakamura
 227 et al., 2013), in our fluid approach we look at the average displacement of magnetic field
 228 lines with respect to their initial distance from the magnetopause. We thus evaluate <

229 $\Delta\psi^2$ \rangle , where the average is on the set of 22500 field lines defined above, $\Delta\psi = \max(\psi) -$
 230 $\min(\psi)$ along a line and where $\sqrt{\langle \Delta\psi^2 \rangle}$ would thus correspond to the average width
 231 of the mixing layer. As shown in Fig.2, panel e, $\langle \Delta\psi^2 \rangle$ grows linearly in time from
 232 $t \simeq 575$ to $t \simeq 675$, indicating a diffusive-type widening of the mixing layer, with an
 233 effective magnetic and matter diffusion coefficient $D_{eff} \simeq 0.1v_{A,z}d_i$. Taking a z -component
 234 of the Alfvén velocity $v_{A,z} \simeq 400 \text{ km/s}$ and $d_i \simeq 300 \text{ km}$ (which corresponds to a KH
 235 wavelength $\lambda_{KH} \simeq 12000 \text{ km}$, as inferred in the MMS event) we obtain $D_{eff} \simeq 10^{10} \text{ m}^2/\text{s}$,
 236 even bigger than the diffusion coefficient needed to account for the observed plasma mix-
 237 ing in a simplified viscous model of the magnetopause (Sonnerup, 1980).

238 Since all new connection changes observed during a given time interval are due to
 239 reconnection events, we can compare the spatial distribution of reconnection sites ob-
 240 tained in our simulation with the ones inferred during the MMS event (Vernisse et al.,
 241 2016). In order to reproduce a magnetopause crossing by a virtual satellite at equato-
 242 rial latitudes, we define three cases: 1) *in-situ* reconnection sites (with respect to the MMS
 243 spacecraft position) when the magnetopause crossing is located around the equators ($-10 d_i <$
 244 $z < +10 d_i$); 2) *remote* sites in the northern hemisphere for a crossing at $z > +10 d_i$;
 245 3) *remote* sites in the southern hemisphere for a crossing at $z < -10 d_i$. These defini-
 246 tions are related to the satellite position, not to the type of reconnection going on. The
 247 results for different time intervals are listed in Tab.1. In agreement with the MMS event
 248 (Vernisse et al., 2016) in the early nonlinear phase ($t \lesssim 600$) the most of the *remote*
 249 reconnection sites are located in the southern rather than in the northern hemisphere.
 250 Note that vortices are expected to be in their early nonlinear phase for this event, as in-
 251 ferred by Nakamura, Hasegawa, et al. (2017) by a careful comparison between their lo-
 252 cal simulation and the MMS observations. Moreover MMS satellites are close to the GSE
 253 equatorial plane (Eriksson et al., 2016), where the growth rate of the KHI is supposed
 254 to be close to its maximum (Vernisse et al., 2016). In our case, this plane correspond to
 255 the $z = 0$ one.

256 In order to interpret the complex topology extrapolated from MMS data, in Fig.3
 257 we draw the density iso-contours corresponding to a 2D chart of vortices in the equa-
 258 torial plane during the early nonlinear phase, together with the intersection points of re-
 259 connected field lines. At $t=550$ black circles symbolize once-reconnected lines, generated
 260 by VIR. These lines intersect the selected plane close to the compressed current sheet
 261 between vortices. The number of these intersection points gradually increases in time

262 along the vortex arms. An “arm” is defined as the low (high) density plasma plume that
 263 is gradually folded into a vortex, e.g. the blue (red) region in between $y \sim 20$ and $y \sim$
 264 40 , at $x \sim 2$ ($x \sim -5$). Since these lines reconnect at $z \lesssim 0$, satellites at $z \simeq 0$ would
 265 measure either in-situ reconnection signatures, for example reconnection outflows and
 266 Hall magnetic field, or accelerated particles streaming parallel to \mathbf{B} (coming from the
 267 south). It is worth noticing that due to the relative motion of vortices during their merg-
 268 ing, the current sheet centered at $y \sim 20$ is more compressed and enhanced as compared
 269 to the one in $y \sim 55$. At later times, $t = 575$, some field lines have also reconnected a
 270 second time also in the northern hemisphere (purple points) and satellites encountering
 271 these twice-reconnected field lines would also observe also antiparallel particle fluxes. Note
 272 that black intersection points are located either close to the compressed current sheet
 273 or along vortex arms while purple points are only located along vortex arms. This kind
 274 of behaviour associated with *remote* mid-latitude reconnection, for which antiparallel fluxes
 275 of accelerated particles from northern reconnection sites could be detected only along
 276 the vortex arms, could help in discerning this type of reconnection mechanism from other
 277 kinds of *remote* reconnection events, such as lobe reconnection (Gosling et al., 1991; Song
 278 & Russell, 1992; Le et al., 1994), for which the intersection points would be equally dis-
 279 tributed between the compressed current sheet and the vortex arms.

280 In the late nonlinear phase, vortices first merge ($t \simeq 600$) and then the single large
 281 vortex turns out to be unstable with respect to secondary KHI ($t \simeq 700$) that devel-
 282 ops at latitudes around $z \simeq 70$. During vortex merging the increase of reconnected lines
 283 is slightly slowed down (Fig.2, panel *c*) while more events are recorded in the northern
 284 hemisphere than in the southern one (see Tab.1). When, for $t \simeq 700$, secondary KHI
 285 grows along the vortex SW arm around $z \simeq 70$, it forces reconnection to occur and boosts
 286 the production of reconnected lines. As a consequence the latitude distribution of recon-
 287 nection sites changes from a two-bump structure (Fig.2, panel *b*, blue line) to a single
 288 wider distribution (panel *b*, red line) with lots of magnetopause crossings from $z \simeq -70$
 289 to $z \simeq 130$.

290 4 Discussion and Summary

291 By performing a 3D two-fluid simulation using the parameters measured by MMS
 292 on September 8th 2015 and using a large numerical box including high-latitude stabi-
 293 lization, we have studied the development of *remote* northern MLR together with vortex-

294 induced reconnection. Even if the North-South symmetry of the system is broken, the
 295 production of twice-reconnected lines turns out to be fairly efficient with 60% of once-
 296 reconnected lines reconnecting a second time. An estimation of the diffusion coefficient
 297 D_{eff} associated with reconnection turns out to be large enough to explain the observed
 298 plasma mixing (Sonnerup, 1980) and compatible with the one inferred by Nakamura, Eriks-
 299 son, et al. (2017); Nakamura, Hasegawa, et al. (2017) where, however, the numerical box
 300 is too small to account for the *remote* dynamics. Two main regimes have been identi-
 301 fied thanks to the analysis of connection changes. In the early nonlinear phase VIR and
 302 northern MLR coexist and generate a latitudinal distribution of connection changes with
 303 two different bumps at different latitudes. Following a virtual satellite around the equa-
 304 torial plane we observe, as found by MMS, more “remote” events in the southern hemi-
 305 sphere than in the northern. However, while Vernisse et al. (2016) identify southern “re-
 306 mote” events as MLR our simulation suggests that they could be related to VIR, which
 307 is found to develop in a wide latitude range reaching into the southern hemisphere.

308 In the late nonlinear phase, as it would be observed by satellites farther tailward
 309 along the magnetopause, vortex merging and secondary KHI develop and force recon-
 310 nection to occur in a wider latitudinal range. In this case the number of reconnection
 311 events becomes larger in the northern hemisphere. Finally, we show a 2D chart of KH
 312 vortices in the equatorial plane with reconnection line intersections, that would help in
 313 discerning MLR from other kinds of *remote* reconnection events in observations. Indeed,
 314 during the early nonlinear phase, particles signatures from *remote* MLR is limited in space
 315 along the vortex arms, while particle signatures from lobe reconnection would intersect
 316 the entire mixing region uniformly.

317 **Acknowledgments**

318 The simulation data are stored in the PIIM laboratory repository and are available at
 319 <https://storagepiim.etoile.univ-amu.fr/share.cgi?ssid=00SbRzp>. The simulations were per-
 320 formed at CINECA (Italy) under the ISCRA initiative.

321 **References**

322 Bavassano Cattaneo, M. B., Marcucci, M. F., Bogdanova, Y. V., Rème, H., Dan-
 323 douras, I., Kistler, L. M., & Lucek, E. (2010). Global reconnection topology
 324 as inferred from plasma observations inside kelvin-helmholtz vortices. Annales

- 325 Geophysicae, 28(4), 893–906. doi: 10.5194/angeo-28-893-2010
- 326 Birn, J., Drake, J. F., Shay, M. A., Rogers, B. N., Denton, R. E., Hesse, M., ...
 327 Pritchett, P. L. (2001). Geospace Environmental Modeling (GEM) Magnetic
 328 Reconnection Challenge. Journal of Geophysical Research: Space Physics,
 329 106(A3), 3715–3719. doi: 10.1029/1999JA900449
- 330 Borgogno, D., Califano, F., Faganello, M., & Pegoraro, F. (2015, March). Double-
 331 reconnected magnetic structures driven by Kelvin-Helmholtz vortices at
 332 the Earth’s magnetosphere. Physics of Plasmas, 22(3), 032301. doi:
 333 10.1063/1.4913578
- 334 Chen, X. L., & Morrison, P. J. (1990, March). Resistive tearing instability with
 335 equilibrium shear flow. Physics of Fluids B: Plasma Physics, 2(3), 495–507.
 336 doi: 10.1063/1.859339
- 337 Contin, J. E. (2003). Theoretical results on the latitude dependence of the
 338 Kelvin-Helmholtz instability at the dayside magnetopause for northward in-
 339 terplanetary magnetic fields. Journal of Geophysical Research, 108(A6). doi:
 340 10.1029/2002JA009319
- 341 Daughton, W., Nakamura, T. K. M., Karimabadi, H., Roytershteyn, V., & Loring,
 342 B. (2014, May). Computing the reconnection rate in turbulent kinetic lay-
 343 ers by using electron mixing to identify topology. Physics of Plasmas, 21(5),
 344 052307. doi: 10.1063/1.4875730
- 345 Eastwood, J. P., Shay, M. A., Phan, T. D., & Øieroset, M. (2010, May). Asym-
 346 metry of the ion diffusion region hall electric and magnetic fields during guide
 347 field reconnection: Observations and comparison with simulations. Phys. Rev.
 348 Lett., 104, 205001. Retrieved from [https://link.aps.org/doi/10.1103/
 349 PhysRevLett.104.205001](https://link.aps.org/doi/10.1103/PhysRevLett.104.205001) doi: 10.1103/PhysRevLett.104.205001
- 350 Eriksson, S., Lavraud, B., Wilder, F. D., Stawarz, J. E., Giles, B. L., Burch, J. L.,
 351 ... Magnes, W. (2016). Magnetospheric Multiscale observations of magnetic
 352 reconnection associated with Kelvin-Helmholtz waves. Geophysical Research
 353 Letters, 43(11), 5606–5615. doi: 10.1002/2016GL068783
- 354 Fadanelli, S., Faganello, M., Califano, F., Cerri, S. S., Pegoraro, F., & Lavraud,
 355 B. (2018, November). North-South asymmetric Kelvin-Helmholtz in-
 356 stability and induced reconnection at the Earth’s magnetospheric flanks.
 357 Journal of Geophysical Research: Space Physics, 123(11), 9340–9356. doi:

358 10.1029/2018JA025626

359 Faganello, M., & Califano, F. (2017, December). Magnetized KelvinHelmholtz insta-
360 bility: theory and simulations in the Earths magnetosphere context. Journal of
361 Plasma Physics, 83(6). doi: 10.1017/S0022377817000770

362 Faganello, M., Califano, F., Pegoraro, F., & Andreussi, T. (2012, December). Double
363 mid-latitude dynamical reconnection at the magnetopause: An efficient mech-
364 anism allowing solar wind to enter the Earth\textquotesingles magnetosphere.
365 EPL (Europhysics Letters), 100(6), 69001. doi: 10.1209/0295-5075/100/69001

366 Faganello, M., Califano, F., Pegoraro, F., Andreussi, T., & Benkadda, S. (2012,
367 November). Magnetic reconnection and KelvinHelmholtz instabilities at the
368 Earth\textquotesingles magnetopause. Plasma Physics and Controlled Fusion,
369 54(12), 124037. doi: 10.1088/0741-3335/54/12/124037

370 Faganello, M., Califano, F., Pegoraro, F., & Retinò, A. (2014, July).
371 Kelvin-Helmholtz vortices and double mid-latitude reconnection at the
372 Earth\textquotesingles magnetopause: Comparison between observa-
373 tions and simulations. EPL (Europhysics Letters), 107(1), 19001. doi:
374 10.1209/0295-5075/107/19001

375 Farrugia, C. J., Gratton, F. T., Bender, L., Biernat, H. K., Erkaev, N. V., Quinn,
376 J. M., ... Dennisenko, V. (1998). Charts of joint Kelvin-Helmholtz and
377 Rayleigh-Taylor instabilites at the dayside magnetopause for strongly north-
378 ward interplanetary magnetic field. Journal of Geophysical Research: Space
379 Physics, 103(A4), 6703–6727. doi: 10.1029/97JA03248

380 Farrugia, C. J., Gratton, F. T., Gnani, G., Torbert, R. B., & Wilson, L. B. (2014).
381 A vortical dawn flank boundary layer for near-radial IMF: Wind observations
382 on 24 October 2001. Journal of Geophysical Research: Space Physics, 119(6),
383 4572–4590. doi: 10.1002/2013JA019578

384 Foullon, C., Farrugia, C. J., Fazakerley, A. N., Owen, C. J., Gratton, F. T., & Tor-
385 bert, R. B. (2008). Evolution of Kelvin-Helmholtz activity on the dusk flank
386 magnetopause. Journal of Geophysical Research: Space Physics, 113(A11). doi:
387 10.1029/2008JA013175

388 Gosling, J. T., Thomsen, M. F., Bame, S. J., Elphic, R. C., & Russell, C. T. (1991).
389 Observations of reconnection of interplanetary and lobe magnetic field lines
390 at the high-latitude magnetopause. Journal of Geophysical Research: Space

- 391 Physics, 96(A8), 14097–14106. doi: 10.1029/91JA01139
- 392 Gratton, F. T., Gnani, G., Farrugia, C. J., & Bender, L. (2003, October). The sta-
393 bility of the pristine magnetopause. Planetary and Space Science, 51(12), 769–
394 783. doi: 10.1016/S0032-0633(03)00113-2
- 395 Hasegawa, H., Fujimoto, M., Phan, T.-D., Reme, H., Balogh, A., Dunlop, M. W., ...
396 TanDokoro, R. (2004). Transport of solar wind into Earth's magnetosphere
397 through rolled-up Kelvin-Helmholtz vortices. Nature, 430(7001), 755. doi:
398 10.1038/nature02799
- 399 Hasegawa, H., Fujimoto, M., Takagi, K., Saito, Y., Mukai, T., & Rme, H. (2006).
400 Single-spacecraft detection of rolled-up Kelvin-Helmholtz vortices at the flank
401 magnetopause. Journal of Geophysical Research: Space Physics, 111(A9). doi:
402 10.1029/2006JA011728
- 403 Hasegawa, H., Retinò, A., Vaivads, A., Khotyaintsev, Y., André, M., Nakamura,
404 T. K. M., ... Seki, Y. (2009). Kelvin-Helmholtz waves at the Earth's mag-
405 netopause: Multiscale development and associated reconnection. Journal of
406 Geophysical Research: Space Physics, 114(A12). doi: 10.1029/2009JA014042
- 407 Hwang, K.-J., Kuznetsova, M. M., Sahraoui, F., Goldstein, M. L., Lee, E., & Parks,
408 G. K. (2011). Kelvin-Helmholtz waves under southward interplanetary mag-
409 netic field. Journal of Geophysical Research: Space Physics, 116(A8). doi:
410 10.1029/2011JA016596
- 411 Johnson, J. R., & Wing, S. (2009). Northward interplanetary magnetic field plasma
412 sheet entropies. Journal of Geophysical Research: Space Physics, 114(A9). doi:
413 10.1029/2008JA014017
- 414 Johnson, J. R., Wing, S., & Delamere, P. A. (2014, November). Kelvin Helmholtz
415 Instability in Planetary Magnetospheres. Space Science Reviews, 184(1), 1–31.
416 doi: 10.1007/s11214-014-0085-z
- 417 Kavosi, S., & Raeder, J. (2015). Ubiquity of Kelvin-Helmholtz waves at Earth's mag-
418 netopause. Nature Communications, 6, 7019. doi: 10.1038/ncomms8019
- 419 Knoll, D. A., & Chacón, L. (2002, May). Magnetic Reconnection in the Two-
420 Dimensional Kelvin-Helmholtz Instability. Physical Review Letters, 88(21),
421 215003. doi: 10.1103/PhysRevLett.88.215003
- 422 Le, G., Russell, C. T., & Gosling, J. T. (1994). Structure of the magnetopause
423 for low Mach number and strongly northward interplanetary magnetic field.

- 424 Journal of Geophysical Research: Space Physics, 99(A12), 23723–23734. doi:
425 10.1029/94JA02182
- 426 Li, L.-X., & Narayan, R. (2004, January). Quasi-periodic Oscillations from Rayleigh-
427 Taylor and Kelvin-Helmholtz Instability at a Disk-Magnetosphere Interface.
428 The Astrophysical Journal, 601(1), 414–427. doi: 10.1086/380446
- 429 Lovelace, R. V. E., Romanova, M. M., & Newman, W. I. (2010, March). Kelvin-
430 Helmholtz instability of the magnetopause of disc-accreting stars. Monthly
431 Notices of the Royal Astronomical Society, 402(4), 2575–2582. doi:
432 10.1111/j.1365-2966.2009.16070.x
- 433 Ma, X., Delamere, P., Otto, A., & Burkholder, B. (2017). Plasma Transport Driven
434 by the Three-Dimensional Kelvin-Helmholtz Instability. Journal of Geophysical
435 Research: Space Physics, 122(10), 10,382–10,395. doi: 10.1002/2017JA024394
- 436 Matsumoto, Y., & Hoshino, M. (2004). Onset of turbulence induced by a
437 Kelvin-Helmholtz vortex. Geophysical Research Letters, 31(2). doi:
438 10.1029/2003GL018195
- 439 Miura, A. (1997, August). Compressible magnetohydrodynamic KelvinHelmholtz
440 instability with vortex pairing in the two-dimensional transverse configuration.
441 Physics of Plasmas, 4(8), 2871–2885. doi: 10.1063/1.872419
- 442 Miura, A., & Pritchett, P. L. (1982). Nonlocal stability analysis of the MHD
443 Kelvin-Helmholtz instability in a compressible plasma. Journal of Geophysical
444 Research: Space Physics, 87(A9), 7431–7444. doi: 10.1029/JA087iA09p07431
- 445 Nakamura, T. K. M., & Daughton, W. (2014). Turbulent plasma transport across
446 the Earth’s low-latitude boundary layer. Geophysical Research Letters, 41(24),
447 8704–8712. doi: 10.1002/2014GL061952
- 448 Nakamura, T. K. M., Daughton, W., Karimabadi, H., & Eriksson, S. (2013, Septem-
449 ber). Three-dimensional dynamics of vortex-induced reconnection and com-
450 parison with THEMIS observations. Journal of Geophysical Research: Space
451 Physics, 118(9), 5742–5757. doi: 10.1002/jgra.50547
- 452 Nakamura, T. K. M., Eriksson, S., Hasegawa, H., Zenitani, S., Li, W. Y., Gen-
453 estreti, K. J., . . . Daughton, W. (2017). Mass and Energy Transfer Across the
454 Earth’s Magnetopause Caused by Vortex-Induced Reconnection. Journal
455 of Geophysical Research: Space Physics, 122(11), 11,505–11,522. doi:
456 10.1002/2017JA024346

- 457 Nakamura, T. K. M., Hasegawa, H., Daughton, W., Eriksson, S., Li, W. Y., & Naka-
458 mura, R. (2017, November). Turbulent mass transfer caused by vortex induced
459 reconnection in collisionless magnetospheric plasmas. Nature Communications,
460 8(1), 1582. doi: 10.1038/s41467-017-01579-0
- 461 Nykyri, K., & Otto, A. (2001). Plasma transport at the magnetospheric bound-
462 ary due to reconnection in Kelvin-Helmholtz vortices. Geophysical Research
463 Letters, 28(18), 3565–3568. doi: 10.1029/2001GL013239
- 464 Pritchett, L. P. (2008, 06). Collisionless magnetic reconnection in an asymmet-
465 ric current sheet. Journal of Geophysical Research, 113. doi: 10.1029/
466 2007JA012930
- 467 Smyth, W. D. (2003, December). Secondary KelvinHelmholtz instability in weakly
468 stratified shear flow. Journal of Fluid Mechanics, 497, 67–98. doi: 10.1017/
469 S0022112003006591
- 470 Song, P., & Russell, C. T. (1992). Model of the formation of the low-latitude
471 boundary layer for strongly northward interplanetary magnetic field.
472 Journal of Geophysical Research: Space Physics, 97(A2), 1411–1420. doi:
473 10.1029/91JA02377
- 474 Sonnerup, B. U. Ö. (1980). Theory of the low-latitude boundary layer. Journal
475 of Geophysical Research: Space Physics, 85(A5), 2017–2026. doi: 10.1029/
476 JA085iA05p02017
- 477 Southwood, D. J. (1968, May). The hydromagnetic stability of the magnetospheric
478 boundary. Planetary and Space Science, 16(5), 587–605. doi: 10.1016/0032
479 -0633(68)90100-1
- 480 Sturmer, A. P., Eriksson, S., Nakamura, T., Gershman, D. J., Plaschke, F., Ergun,
481 R. E., ... Burch, J. L. (2018, Feb). On multiple hall-like electron currents
482 and tripolar guide magnetic field perturbations during kelvin-helmholtz waves.
483 Journal of Geophysical Research (Space Physics), 123(2), 1305-1324. doi:
484 10.1002/2017JA024155
- 485 Vernisse, Y., Lavraud, B., Eriksson, S., Gershman, D. J., Dorelli, J., Pollock,
486 C., ... Yokota, S. (2016). Signatures of complex magnetic topologies
487 from multiple reconnection sites induced by Kelvin-Helmholtz instability.
488 Journal of Geophysical Research: Space Physics, 121(10), 9926–9939. doi:
489 10.1002/2016JA023051

490 Walker, A. D. M. (1981, October). The Kelvin-Helmholtz instability in the low-
491 latitude boundary layer. Planetary and Space Science, 29(10), 1119–1133. doi:
492 10.1016/0032-0633(81)90011-8

Table 1. Number of *in-situ* and *remote* events.

Time interval	Southern h.	<i>In-situ</i>	Northern h.
501-525	35	81	2
526-550	377	201	7
551-575	677	321	327
576-600	730	268	590
601-625	544	145	686
626-650	694	247	953
651-675	488	356	1346
676-700	147	328	747
701-725	-	120	757
726-750	650	-	1656

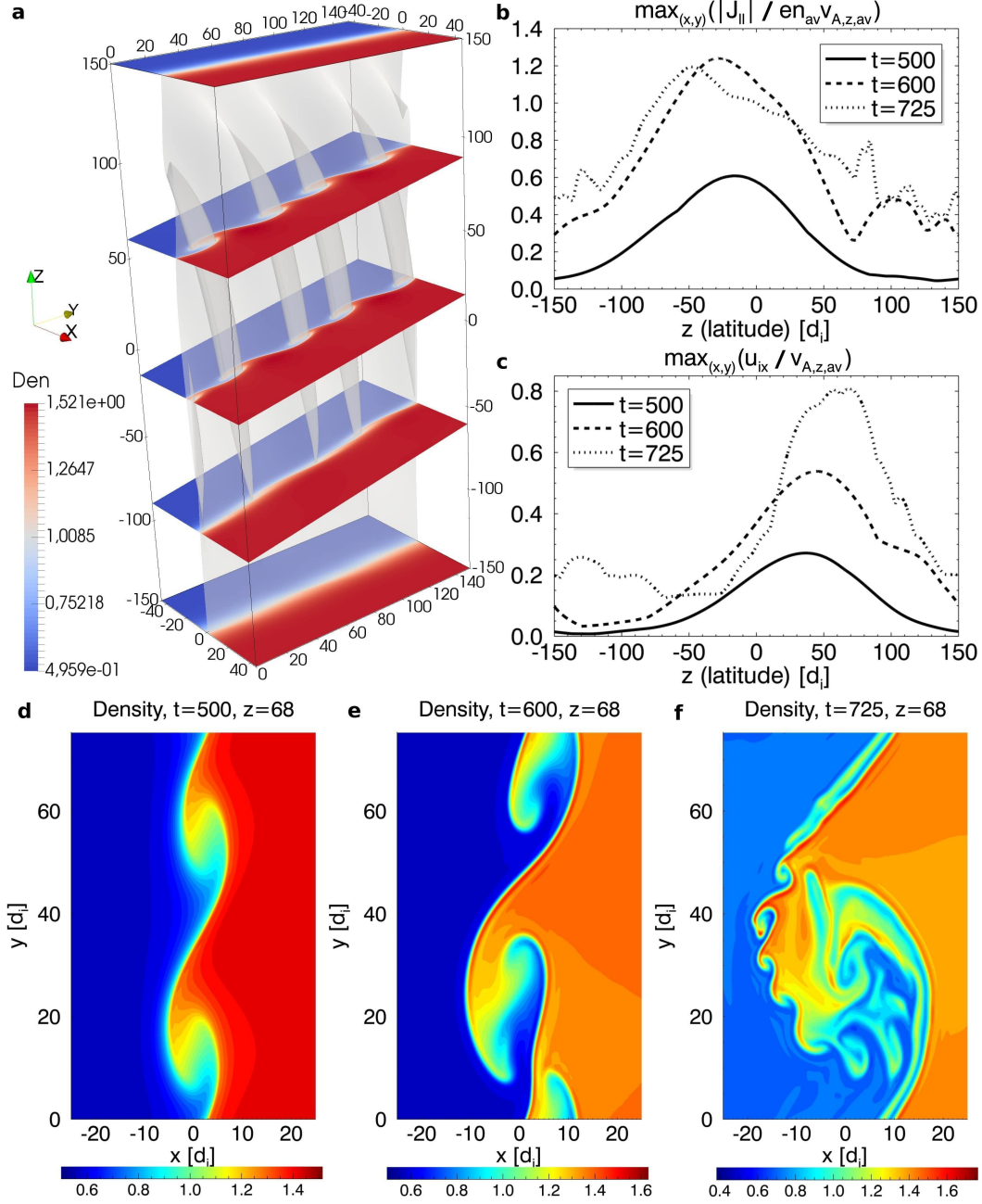


Figure 1. Panel *a*: 3D rendering of KH vortices at $t = 525$. Blue and red colors represent plasma density (red high-density, blue low-density). The grey shaded surface, $\psi = 0$, corresponds to the magnetopause. The three central planes are perpendicular to the vortex axis. The box has been doubled along y -direction for sake of clearness. Panel *b*, *c*: plot of $\max_{(x,y)}(|J_{\parallel}|)$ and of $\max_{(x,y)}(u_{ix})$ as a function of z at $t = 500$ (dashed), $t = 600$ (dotted), $t = 725$ (continuous). Panels *d*, *e*, *f*: density iso-contours at the latitude $z = 68$ for three different times $t = 500$, $t = 600$ and $t = 725$.

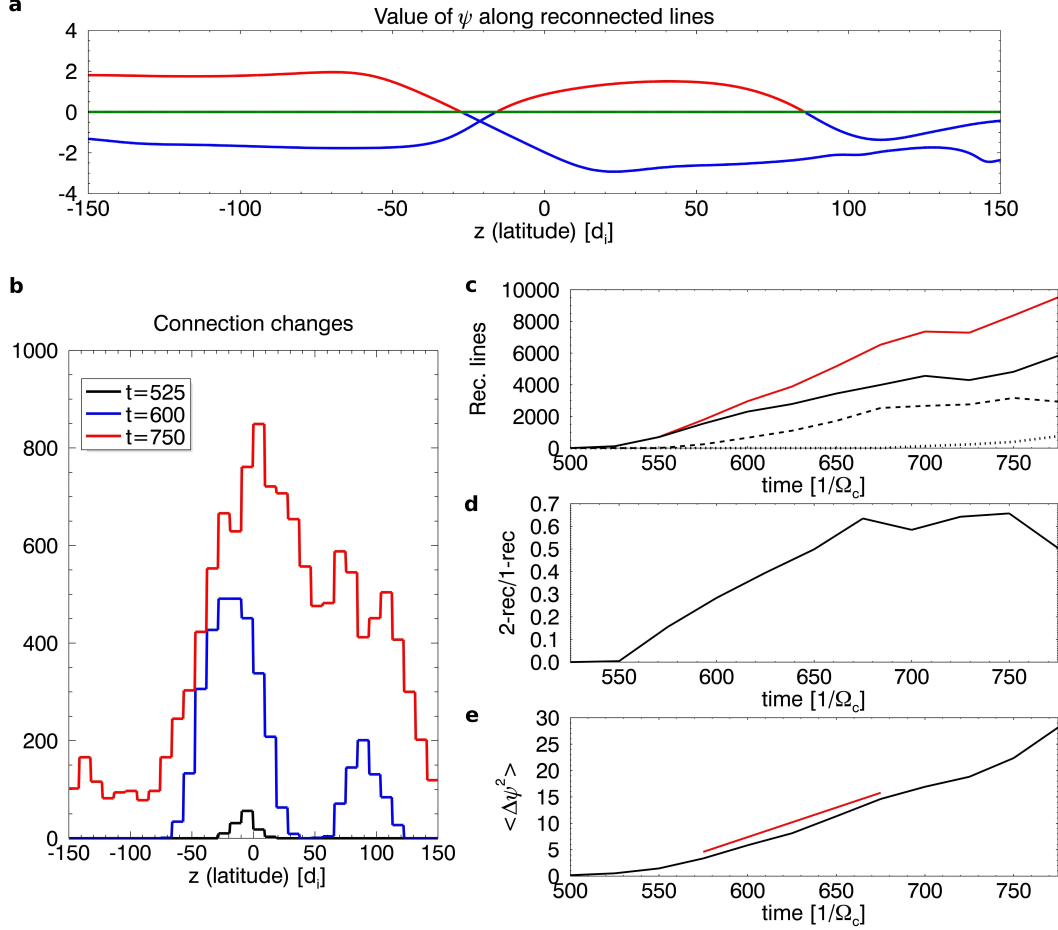


Figure 2. Panel *a*: ψ as a function of z for two chosen magnetic field lines at $t = 600$. Blue and red colors are set according to the plasma lines are connected to. The green line represents the magnetopause. Panel *b*: latitudinal distribution of connection changes at $t = 525$ (black), $t = 600$ (blue) and, finally, $t = 750$ (red). Panel *c*: time evolution of the total number of reconnected field lines (red), once (black), twice (black dashed) and 2^+ -reconnected (black dotted) lines. Panel *d*: time evolution of the ratio between twice-reconnected and once-reconnected lines. Panel *e*: time evolution of $\langle \Delta\psi^2 \rangle$, the slope 0.1 (red) is given as reference.

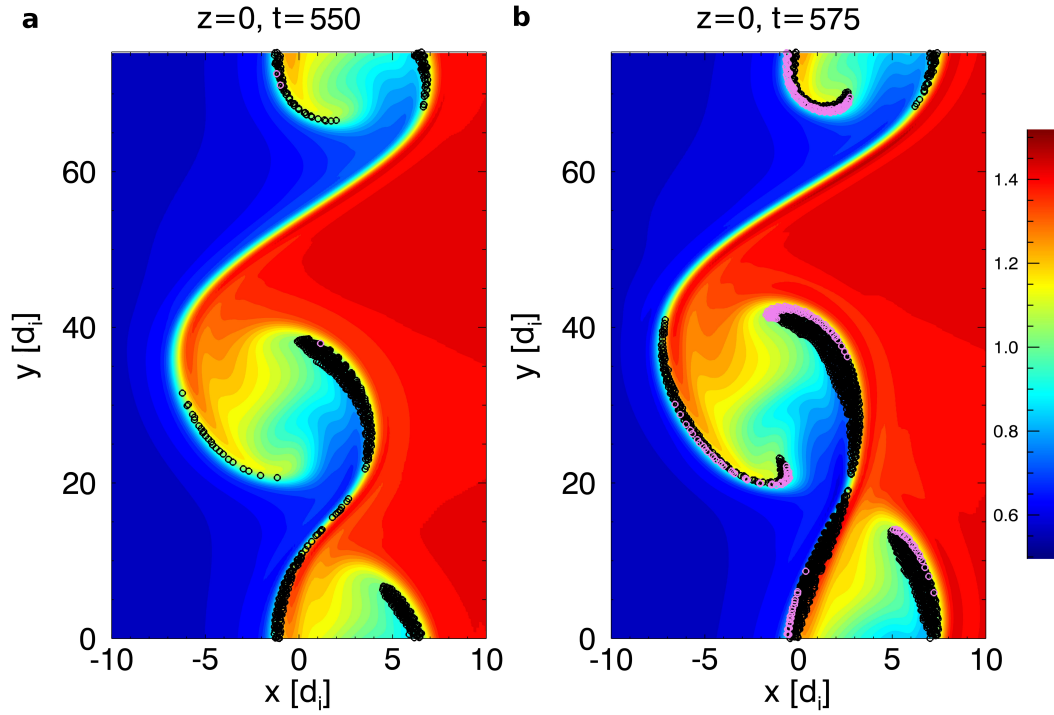


Figure 3. Density iso-contours at $z = 0$ (red high-density, blue low-density) and positions of the intersection points of the reconnected field lines in the equatorial plane ($z = 0$) at $t = 550$ (panel *a*) and $t = 575$ (panel *b*). In black once-reconnected lines, in purple twice-reconnected ones.